Single-Crystalline Bilayered V_2O_5 Nanobelts for High-Capacity Sodium-Ion Batteries

Dawei Su and Guoxiu Wang*

Centre for Clean Energy Technology, School of Chemistry and Forensic Science, Faculty of Science, University of Technology, Sydney, NSW 2007, Australia

ABSTRACT Single-crystalline bilayered vanadium oxide nanobelts were synthesized by a simple solvothermal method. FESEM and AFM analyses identified the nanobelt morphology of the as-prepared vanadium oxide with a rectangular cross-section and a thickness of approximately 50 nm. XRD and TEM characterizations revealed the presence of a large (001) interlayer spacing (~11.53 Å), which can accommodate Na-ion insertion and extraction. When applied as cathode materials in Na-ion batteries, vanadium oxide nanobelts exhibited a high capacity of 231.4 mA h g^{-1} at a current density of 80 mA g^{-1}. This corresponds to the theoretical capacity to form $Na_2V_2O_5$ on Na-ion insertion. Vanadium oxide nanobelts also demonstrated an excellent high-rate performance and a satisfactory cyclability. These superior electrochemical performances could be ascribed to the unique bilayered vanadium oxide nanobelts with dominantly exposed {100} crystal planes, which provide large interlayer spacing for facile Na-ion insertion/extraction. Single-crystalline bilayered vanadium oxide nanobelts could be promising cathode materials for high-performance Na-ion batteries.

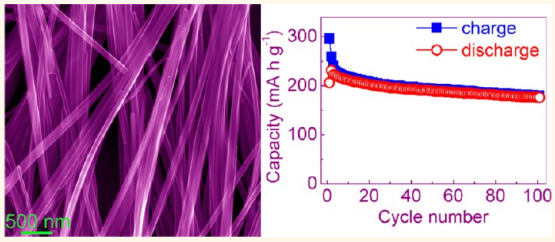

KEYWORDS: vanadium oxide nanobelt · bilayered structure · cathode material · sodium-ion battery

Na-ion batteries, as an alternative to Li-ion batteries,[1,2] have attracted extensive investigations,[3,4] owing to abundant supply and widespread terrestrial reserves of sodium mineral salts. Much progress on developing cathode materials for Na-ion batteries has been achieved. For example, Zaghib *et al.* reported the synthesis of olivine $NaFePO_4$ (a framework material based on the phosphate polyanion) and obtained a specific capacity of 147 mA h g^{-1}.[5] However, its reversibility is very poor (50.6 mA h g^{-1} in the second cycle). Fluoride-based cathode materials ($NaMF_3$, M = Fe, Mn, V, and Ni) have been prepared with specific capacities ranging from 30 to 170 mA h g^{-1}.[6,7] Moreover, layered transition metal oxides, such as P2-Na_xCoO_2,[8,9] P2-$Na_{2/3}[Fe_{1/2}Mn_{1/2}]O_2$,[10] $Na_{2/3}(Ni_{1/3}Fe_{1/3}Mn_{2/3})O_2$,[11] $NaCrO_2$,[12,13] Na_xMnO_2,[14,15] and Na_xVO_2,[16] with stable capacities were reported. Fluorophosphate and fluorosulfate materials were also developed as cathode materials for Na-ion batteries.[17−20] We have successfully prepared α-MnO_2, β-MnO_2,[21] and $Na_{0.7}MnO_2$[22] as cathode materials for Na-ion batteries. Rechargeable Li-ion or Na-ion batteries rely on a metal oxide cathode host, from and into which alkali ions can be inserted and extracted reversibly.[23−29] The lithium ion is small enough to have an acceptable mobility and a solid-solution range in close-packed oxide−ion arrays. However, the larger sodium ion and its higher ionization potential require a more open framework for Na-ion intercalation and deintercalation.[11−30] On the basis of this principle, the NASICON structured $Na_{1+3x}Zr_2(P_{1-x}Si_xO_4)_3$ with the hexagonal framework exhibited fast sodium-ion conductivity due to its unique open-frame $M_2(XO_4)_3$ structure.[31] However, the $M_2(XO_4)_3$ units in the framework are rotated to induce a monoclinic structure, and the substitution of a transition metal of interest for Zr(IV) generates a monoclinic structure when Na^+ is the guest alkali ion, resulting in the decrease of sodium-ion mobility.[32] Alternatively, the Goodenough group successfully prepared the $KMFe(CN)_6$ compounds (M = transition-metal ions: Mn, Fe, Co, Ni, and Zn),[33] which have a cubic framework with M(II) and Fe(III) on alternate corners of a cube of corner-shared octahedra bridged

* Address correspondence to Guoxiu.Wang@uts.edu.au.

Received for review September 26, 2013 and accepted November 9, 2013.

Published online November 09, 2013
10.1021/nn405014d

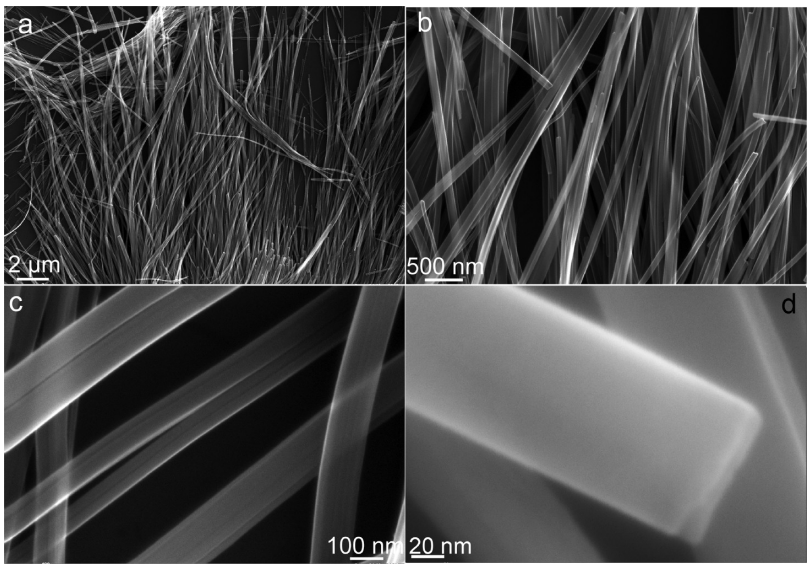

Figure 1. FESEM images of bilayered V_2O_5 nanobelts. (a and b) Low-magnification images, showing homogeneous shape and size distribution of nanobelts. (c and d) High-magnification images, which illustrate the features of individual V_2O_5 nanobelts.

by linear $(C{\equiv}N)^-$ anions. This crystal structure opens the elementary cubes for sodium ion to move between half-filled body-centered positions. Although the materials in this family demonstrated good reversibility as electrode materials in Na-ion batteries, they suffered from low specific capacity (about 100 mA h g^{-1}). Therefore, it is challenging to discover other high-capacity cathode materials with open-framework structures for Na-ion batteries. Vanadium pentoxide (V_2O_5) has been investigated as cathodes for Li-ion batteries[34−36] and supercapacitors.[37] The layered structure of V_2O_5 could facilitate Li-ion insertion and extraction.[38] It has been reported that the bilayered V_2O_5 with larger *d*-spacing than orthorhombic V_2O_5 achieved a good electrochemical performance as cathodes in Na-ion batteries.[39]

In this study, we report the successful synthesis of single-crystalline bilayered vanadium oxide nanobelts with large interlayer spacing of (001) crystal planes (~11.53 Å). Vanadium oxide nanobelts exhibited a high capacity of 231.4 mA h g^{-1}, an excellent high-rate performance, and a satisfactory cycling performance.

RESULTS AND DISCUSSION

Phase, Morphology, and Structure Characterization. The morphology of the as-prepared vanadium oxide nanobelts was observed by field emission scanning electron microscopy (FESEM). As shown in Figure 1, the low-magnification SEM images (Figure 1a and b) show that the product consists of 100% one-dimension (1D) nanobelts with a homogeneous size and shape distribution. The lengths of V_2O_5 nanobelts extend to a few micrometers. The high-magnification FESEM images (Figure 1c and d) clearly confirmed the nanobelt feature of vanadium oxide, with a rectangle cross-section (Figure 1d). The width of the V_2O_5 nanobelt is

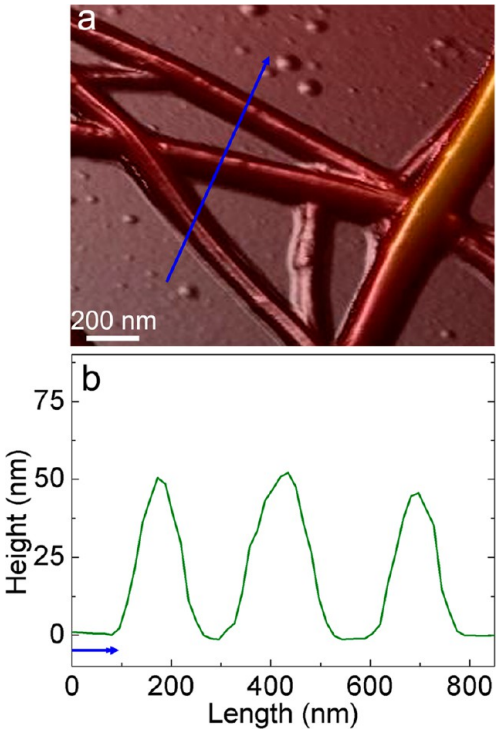

Figure 2. AFM image of the 1D bilayered V_2O_5 nanobelts' topography (a) and corresponding height profiles (b).

estimated to be about 90 nm. AFM measurement was conducted to observe the topography of V_2O_5 nanobelts (as shown in Figure 2a). From the scanning profile of three V_2O_5 nanobelts, we can determine the height of V_2O_5 nanobelts to be about 50 nm.

The phase of vanadium oxide nanobelts was identified by X-ray diffraction (XRD) (Figure 3a) and refined by the Rietveld method[40,41] (as implemented by the GSAS software suite) between 5° and 90°. The possible structural model is shown in Figure 3b−d. The lattice

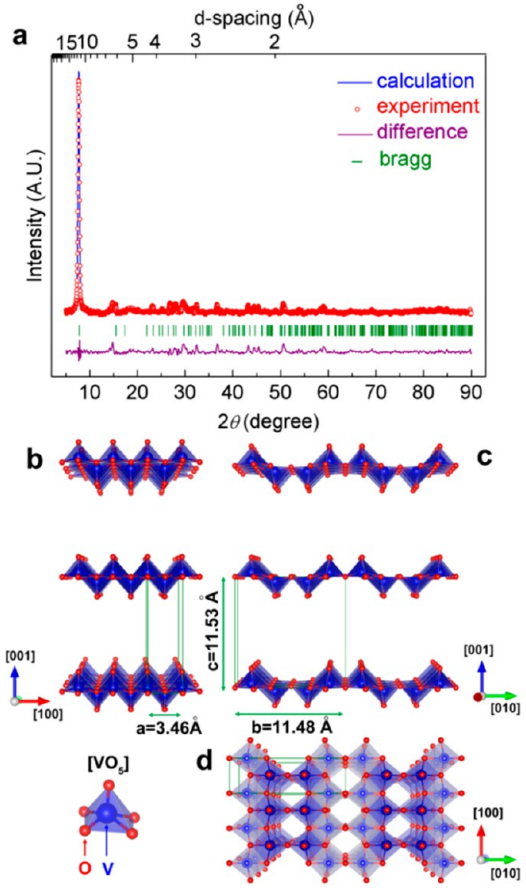

Figure 3. (a) X-ray diffraction pattern and Rietveld refinement of as-prepared V_2O_5. The observed and calculated intensities are represented by red dots and a blue solid line, respectively. The bottom purple line shows the fitting residual difference. Bragg positions are represented by light green ticks. (b–d) Refined structural model of the bipyramidal layered structure of V_2O_5 viewed along the [010] (b), [$\bar{1}$00] (c), and [001] (d) directions. The blue base-faced square-pyramidal VO_5 unit consists of one vanadium atom and five oxide atoms, which are colored blue and red, respectively.

parameters were calculated as a = 3.4607(3) Å, b = 11.4817(4) Å, c = 11.5324(5) Å, α = 89.9713(6)°, and β = 89.9003 (2)° (triclinic, space group $P1$), with satisfactory convergence factors (χ^2 = 8.5, R_{wp} = 10.36%, R_p = 9.32%). This result is consistent with a previously reported bipyramidal layered structure of V_2O_5.[39] As indicated by narrow features in the XRD diffraction peak at the low d-spacing range of the diffraction patterns, it can be concluded that the as-prepared V_2O_5 nanobelts do have large intercalation space in the crystal structure, which was confirmed by the d-spacing-dependent XRD patterns (the top axis of Figure 1a and Figure S1 in the Supporting Information). This crystal structure consists of 2D bilayered stacks, separated by large interlayer spacing, which corresponds to a strong diffraction peak at 2θ = 7.7° with a d-spacing of 11.53 Å. As illustrated in Figure 3b–d, base-faced square-pyramidal VO_5 units are arranged in parallel at positions of equal distance. There are two V_2O_5 units per unit cell, which are built up from distorted trigonal bipyramidal coordination polyhedra of O around V, sharing edges to form $(V_2O_4)_n$ zigzag double chains along the [100] direction and cross-linking along the [010] direction through shared corners. This leads to the formation of sheets in the ab-plane (Figure S2). Along the c-axis, the as-prepared V_2O_5 presents a noticeable distance between the closest approach bilayer stacks (~11.53 Å), which is more than twice those of the orthorhombic V_2O_5 (Figure S3). This unique crystal structure renders the bilayered V_2O_5 as potential cathode materials for Na-ion batteries.

The formation of a large interlayer distance in the as-prepared bilayered V_2O_5 nanobelts could be associated with the chemisorption of preferred molecules.[42] When deionized water was used as solvent without the pyridine additive during the synthesis, the final products were orthorhombic V_2O_5 powders with the space group $Pmmn$ (a = 11.516, b = 3.5656, and c = 4.3727 Å), as shown in Figure S3 and Figure S4.

The bilayered V_2O_5 nanobelts were further characterized by Raman and Fourier transform infrared (FT-IR) spectra and compared with orthorhombic V_2O_5 (Figure 4). Figure 4a shows the crystal structure model of V_2O_5 nanobelts. In each sheet layer (along the ab-plane), V is 6-fold coordinated. These include (i) three V–O bonds (d_1, d_2, and d_3 with 1.78, 1.88, and 2.03 Å bond length, respectively, involving 3-fold-coordinated oxygens belonging to V_2O_4 chains (Oc)), (ii) one V–O bond (d_4) of 1.77 Å (involving 2-fold-coordinated oxygen constituting bridges between two chains (O_B)), and (iii) one short V–O bond (d_5) of 1.54 Å (involving the apex oxygen (O_A)) and one long V–O bond (d_6) of 9.99 Å bond length, involving the O_A oxygen atoms, which ensures the cohesion of two successive layers. Under the D_{2h} factor group (k = 0), the crystal modes can be classified as 21 Raman- and 15 IR-active modes.[43,44] Raman scattering spectra are shown in Figure 4b. Generally, both bilayered V_2O_5 and orthorhombic V_2O_5 display a similar spectrum. The predominant low-wavenumber bond at 146 cm^{-1} is attributed to the skeleton bent vibration, which is a characteristic of the layer-type structure of V_2O_5. The peaks at 198 and 286 cm^{-1} are originated from the bending vibrations of the O_C–V–O_B bond. The bending vibration of V–O_C, the bending vibration of the V–O_B–V bond, and the stretching vibration of the V–O_C bond occur at about 300, 404, and 706 cm^{-1}, respectively.[45,46] Moreover, the peak at 995 cm^{-1}, which is associated with the vanadyl mode, corresponds to the stretching of vanadium atoms connected to oxygen atoms by double bonds.[45,47,48] The skeleton bent vibration at 146 cm^{-1} and the stretching vibration of vanadyl V=O_A at 995 cm^{-1} are the fingerprints of the perfect layer-type structure of V_2O_5. It should be noticed that the as-prepared bilayered V_2O_5 presents reduced

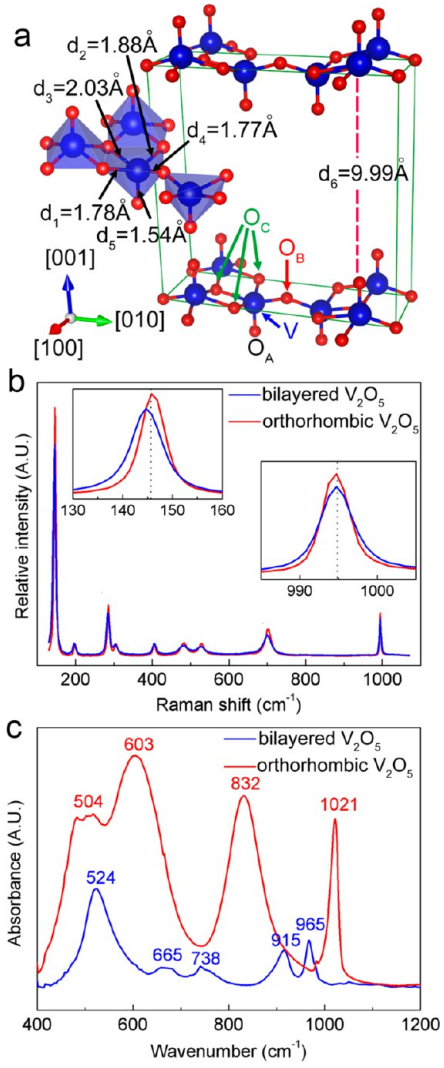

Figure 4. (a) Bilayered V_2O_5 crystal structure, in which the 6-fold-coordinated V and three structurally different oxygen atoms are presented. (b) Raman scattering spectra of bilayered and orthorhombic V_2O_5. Insets are the magnified scale spectra. (c) FT-IR spectra of bilayered and orthorhombic V_2O_5.

intensities of these two peaks (as shown by insets in Figure 4b), compared with orthorhombic V_2O_5. This indicates that the structure of bilayered V_2O_5 is distorted, which could be due to the increase of the (001) crystal plane distance, because the d_6 bond of bilayered V_2O_5 is larger (9.99 Å) than the counterpart in orthorhombic V_2O_5 (2.8 Å, Figure S5).[49]

The FT-IR spectrum of bilayered V_2O_5 nanobelts is different from that of orthorhombic V_2O_5 (as shown in Figure 4c). The orthorhombic V_2O_5 exhibits four main vibration modes in the 400−1200 cm^{-1} region: the terminal oxygen symmetric stretching mode (ν_s) of V═O_A (1021 cm^{-1}), the 3-fold-coordinated oxygen asymmetric stretching mode (ν_{as}) of V−O_C−V (603 cm^{-1}), and the bridge oxygen asymmetric and symmetric stretching modes (ν_{as} and ν_s) of V−O_B−V (832 and 504 cm^{-1}, respectively).[48] While the FT-IR spectrum of bilayered V_2O_5 shows peaks at 524, 665, 738, 915, and 965 cm^{-1}, the ν_{as}(V−O_C−V), ν_s(V−O_B−V), and ν_{as}(V−O_B−V) modes shift to higher wavenumbers (665, 915, and 524 cm^{-1}, respectively) with decreased intensities. Furthermore, the ν_s(V═O) band slightly shifts to a lower wavenumber from 1021 cm^{-1} to 965 cm^{-1}. The symmetric stretching mode ν_s(V−O_C−V) at 738 cm^{-1} appears in the spectrum. The changes of vibration modes should be ascribed to the change of V_2O_5 crystal structure, especially the large interlayer distance along the *c*-axis, which results from more H atoms bonding with O_A atoms due to the H-bonding effects.[50] Consequently, it will decrease the strength of the V═O_A bonds and, correspondingly, strengthen the V−O_B−V bond,[51] leading to the shift of the bond vibration.

The detailed crystal structures of the bilayered V_2O_5 nanobelts were characterized by transmission electron microscopy (TEM), high-resolution TEM (HRTEM), and selected area electron diffraction (SAED) analyses (Figure 5). From the typical low-magnification TEM images (Figure 5a and Figure S6), it can be confirmed that the as-prepared bilayered V_2O_5 nanobelts present the well-separated free-standing feature for individual nanobelts. The SAED patterns (the inset in Figure 5b and Figure 5d) verified the single-crystalline nature of V_2O_5 nanobelts. All SAED spot patterns can be fully indexed along the [100] zone axis, from which we can determine that V_2O_5 nanobelts grow along the [010] direction. Through the lattice resolved HRTEM image (Figure 5c), the 11.5 Å distance of the interlayer along the *c*-axis was identified. From the atomic resolution HRTEM image (Figure 5e), we can directly observe the interlayer gap of the (100) crystal plane, which corresponds to the large distance between bilayer stacks along the [001] direction, as illustrated by the simulated (100) V_2O_5 crystal plane (inset in Figure 5e). Furthermore, combining the rectangular cross-section architecture of V_2O_5 nanobelts (as determined by FESEM and AFM analyses), it can be concluded that the as-prepared bilayered V_2O_5 nanobelts are enclosed by the {100}, {001}, and {010} crystal planes (as illustrated by the geometric model in Figure 5f). Obviously, the {100} facets are the predominantly exposed facets on which the large interlayers between the (001) crystal planes provide a facile channel for Na-ion diffusion. Moreover, the small height (approximate 50 nm) of the as-prepared V_2O_5 nanobelts can shorten the sodium ion's diffusion distance when applied as electrodes in Na-ion batteries.

Electrochemical Properties of Bilayered V_2O_5 Nanobelts for Na-Ion Batteries. When the bilayered V_2O_5 nanobelts were used as cathodes in Na-ion batteries, the electrochemical performances were evaluated by galvanostatic charge and discharge cycling. Figure 6a shows charge−discharge profiles tested at 80 mA g^{-1}. The as-prepared bilayered V_2O_5 nanobelts delivered an initial

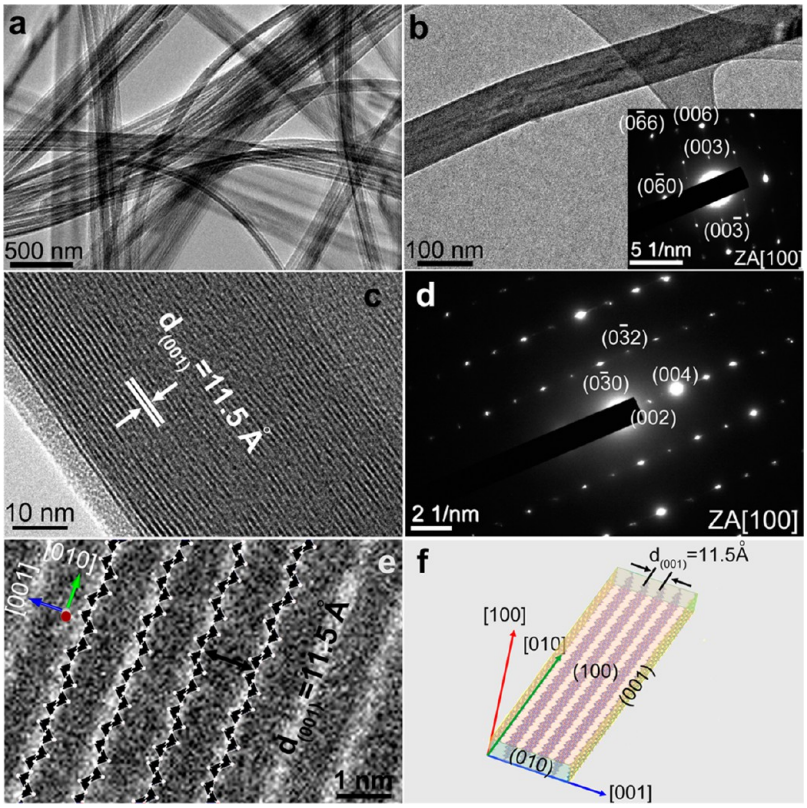

Figure 5. (a) Low-magnification TEM image of typical free-standing V_2O_5 nanobelts. (b) High-magnification TEM image of an individual V_2O_5 nanobelt. Inset is its corresponding selected area electron diffraction (SAED) spot patterns. (c) Lattice resolution TEM image, in which the (001) crystal plane can be identified. (d) Corresponding SAED spot patterns of c, further signifying its single-crystal feature. (e) Atomic resolution HRTEM image of a V_2O_5 nanobelt, from which the interlayer structure of the bilayered V_2O_5 can be directly observed. Inset of e is the simulated V_2O_5 (100) crystal plane, which demonstrates the distance of adjacent layers of V_2O_5 along the *c*-axis (V and O atoms are marked as black and white color, respectively). (f) Geometrical model of as-prepared bilayered V_2O_5 nanobelts, in which enclosed crystal planes ((100), (010), and (001)) are colored differently.

discharge capacity of 206.3 mA h g^{-1} with a voltage plateau at about 2.4 V. It should be noted that the discharge profiles in the second and third cycles are different from those of the first one, with increased capacities (231.4 and 222.9 mA h g^{-1}, respectively). We proposed that electrolyte gradually diffused into the large space between bilayer stacks along the [001] direction in the first cycle. Consequently, the electrolyte between the stacks will facilitate the electrochemical reaction, leading to the increase of capacity in the subsequent cycles. This phenomenon is similar to mesoporous structured electrode materials, in which capacity increases with cycling in the initial few cycles.[52] The irreversible capacity in the first cycle could originate from the reaction of the cathode surface with the electrolyte, particularly with the high cutoff charge voltages of 4.0 V.[53] Two discharge plateaus were observed in the discharge voltage profiles (Figure 6a). The discharge plateau at 2.5−2.3 V corresponds to sodium-ion insertion into the lattice framework of V_2O_5 nanobelts, which is similar to the previous report on the tunnel structured cathode material.[54] The discharge plateau at 1.5−1.2 V could be ascribed to the formation of the solid electrolyte interphase (SEI) layer on the surface of the electrode.[55,56] The high capacity of bilayered V_2O_5 nanobelts is close to the theoretical capacity (236 mA h g^{-1}) for the formation of $Na_2V_2O_5$, in which each unit cell can accommodate approximately two sodium ions.[39] The bilayered V_2O_5 nanobelts demonstrated a stable cycling performance. The electrode still delivered a discharge capacity of 170 mA h g^{-1} after 100 cycles (Figure 6b). We also cycled bilayered V_2O_5 nanobelt electrodes at different current densities: 40, 160, 320, and 640 mA g^{-1}. As shown in Figure 7a, bilayered V_2O_5 nanobelt electrodes achieved high discharge capacities of 235.7, 195.7, 151.2, and 134 mA h g^{-1}, respectively, in the second cycle.

After 100 cycles, the discharge capacities were maintained at high values when cycled at different current densities. To evaluate the tolerance toward varied current densities of bilayered V_2O_5 nanobelts, a stepwise density test was conducted. As shown in Figure 7b, the electrode recovered to the high values as long as the current density reversed back to low current densities. In comparison, the orthorhombic V_2O_5 as cathodes was also tested under the same measurement conditions (Figure S9). Orthorhombic

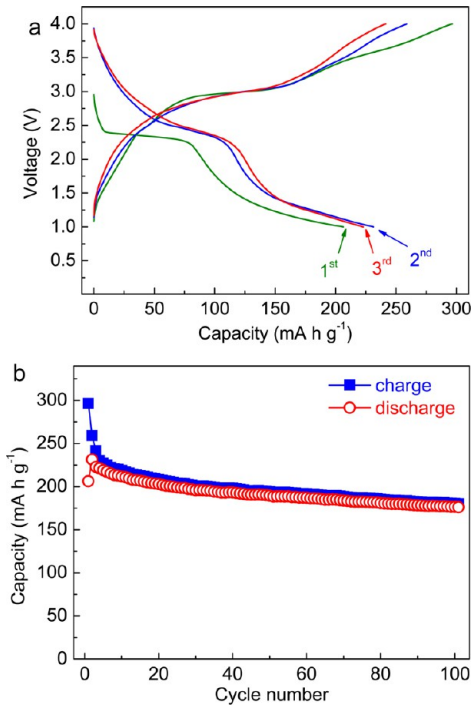

Figure 6. (a) First, second, and third discharge and charge profiles of bilayered V_2O_5 nanobelt at 80 mA g^{-1} current density. (b) Charge and discharge capacities *versus* cycle number at current densities of 80 mA g^{-1}.

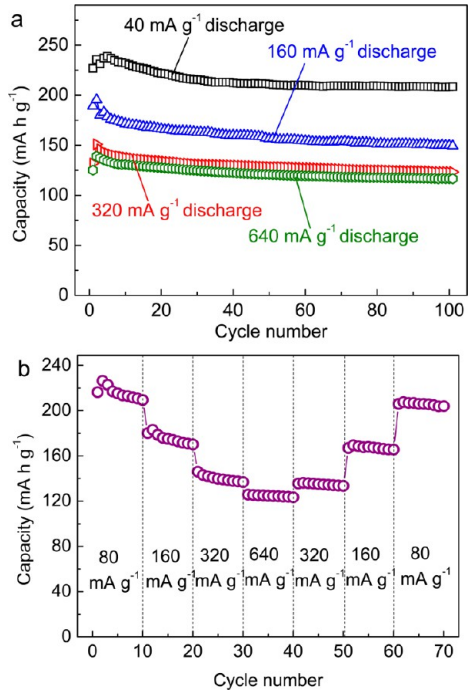

Figure 7. (a) Discharge capacities *versus* cycle number at current densities of 40, 160, 320, and 640 mA g^{-1}. (b) Rate performance of a bilayered V_2O_5 nanobelt at varied current densities.

V_2O_5 powders exhibited much lower capacities and poor cycling performances.

To further understand the mechanism of sodium-ion insertion in bilayered V_2O_5 nanobelts, an *ex-situ*

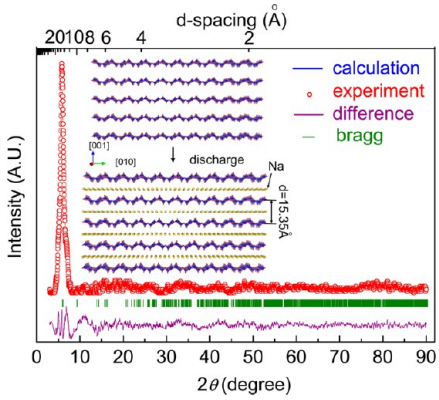

Figure 8. X-ray diffraction patterns and Rietveld refinement of V_2O_5 after the first discharge process. The observed and calculated intensity are represented by red dots and a blue solid line, respectively. The bottom purple line shows the fitting residual difference. Bragg positions are represented by light green ticks. The inset is the demonstration of a refined structural model of a bipyramidal V_2O_5 layered structure after insertion of sodium ions, with the increased bilayer distance (15.35 Å), viewed along the [100] directions. The blue base-faced square-pyramidal VO_5 unit is composed of one vanadium atom and five oxide atoms, which are colored blue and red, respectively, while the sodium ions are colored yellow.

XRD measurement was performed. We monitored the structural change of bilayered V_5O_2 nanobelts at the fully discharged status. As shown in Figure 8, only the (001) diffraction peak at 5.7° is well-defined. All other diffraction peaks are broad and weak. No new phase was detected at the fully discharged state. The lattice parameters were refined to be a = 3.3904(4) Å, b = 12.0317(1) Å, and c = 15.3531(5) Å, based on the $Na_2V_2O_5$ crystal structure with the convergence factors of χ^2 = 10.2, R_{wp} = 15.03%, and R_p = 13.68%. Due to the intercalation of sodium ions, the unit cell has expanded. In particular, the interlayer spacing of the (001) crystal plane has expanded from 11.5324 to 15.3531 Å (as illustrated by the *d*-spacing-dependent XRD patterns: top axis in Figure 8 and Figure S10).

The superior electrochemical performance of bilayered V_2O_5 nanobelts as cathode material in Na-ion batteries could be ascribed to the unique crystal structure with large interlayer spacing. Moreover, V_2O_5 nanobelts contain predominantly exposed (100) facets, on which the large (001) interlayer spacings are exposed to the surface. This crystal structure provides open channels for facile Na-ion insertion and extraction, which is similar to the previously reported $LiMn_2O_4$ nanotubes with some excellent eletrochemical performances due to the preferred orientation.[57] The thin nanobelt morphology (~50 nm in thickness) also offers a short path for Na ion diffusion in the V_2O_5 crystal structure, leading to an excellent high-rate performance.

CONCLUSION

Bilayered V_2O_5 nanobelts were successfully synthesized by a solvothermal method. FESEM and atomic

force microscopy (AFM) observation confirmed the nanobelt morphology of the V_2O_5 product. XRD, Raman, FT-IR, and TEM revealed that the bilayered V_2O_5 nanobelts have a large *d*-spacing of (001) crystal planes with an interlayer distance of 11.53 Å. Furthermore, bilayered V_2O_5 nanobelts consist of predominantly exposed (100) facets, on which the large *d*-spacings of the (001) planes are perpendicular to them. This unique crystal structure provides exposed channels for facile Na-ion insertion and extraction. When applied as cathode materials in Na-ion batteries, bilayered V_2O_5 nanobelts exhibited a high discharge capacity of 231.4 mA h g^{-1}, corresponding to the formation of $Na_2V_2O_5$. This has been verified by the *ex-situ* XRD analysis. Moreover, bilayered V_2O_5 nanobelts also demonstrate an excellent high-rate capacity and a satisfactory cycling performance.

EXPERIMENTAL SECTION

Synthesis of Bilayered V_2O_5 Nanobelts. Bilayered V_2O_5 nanobelts were synthesized by a hydrothermal method. In a typical synthesis process, 1 mmol of VCl_3 (Sigma-Aldrich, ≥ 97%) was dissolved in a mixture of pyridine (5 mL, Sigma-Aldrich) and deionized water (10 mL) under vigorous stirring at room temperature. After that, the precursor solution was heated at 160 °C in a Teflon-lined autoclave (25 mL in capacity) for 12 h. The precipitate was cooled to room temperature naturally, collected, and washed with deionized water and ethanol several times. After drying at 100 °C in a vacuum oven overnight, the final products were obtained. The orthorhombic V_2O_5 powders were also prepared by the same procedure, but without pyridine in the solvent.

Structural and Physical Characterization. The crystal structure and phase of the as-prepared materials were characterized by X-ray diffraction (Siemens D5000) using Cu Kα radiation (operation voltage 40 kV, current 20 mA) at a very slow scanning step of 0.0025° s^{-1} (9.67 h from 3° to 90°). Rietveld refinement was implemented using the GSAS software suite.[33] The morphology was analyzed by FESEM (Zeiss Supra 55VP). The structure details were further characterized by TEM and HRTEM (JEOL JEM-2011). SAED patterns were recorded by a Gatan CCD camera in a digital format. The thickness of as-prepared bilayered V_2O_5 nanobelts was measured by AFM using a Bruker Dimension 3100 instrument under a MicroMasch NSC16 tip with 40 N m^{-1} of spring constant. The AFM sample was deposited on the silicon substrate for AFM measurement. Raman spectra were measured using a Renishaw inVia Raman spectrometer system (Gloucestershire, UK) equipped with a Leica DMLB microscope (Wetzlar, Germany) and a 17 mW at 633 nm Renishaw helium neon laser source. FT-IR spectra were recorded on a Nicolet Magna 6700 FT-IR spectrometer with 0.9 cm^{-1} standard optical resolution by using a KBr beam splitter.

Electrochemical Testing. The electrodes were prepared by dispersing the as-prepared bilayered V_2O_5 nanobelts (70 wt %), acetylene carbon black (20 wt %), and poly(vinylidene fluoride) binder (10 wt %) in *N*-methyl-2-pyrrolidone to form a slurry. The resultant slurry was pasted onto aluminum foil using a doctor blade and dried in a vacuum oven for 12 h, followed by pressing at 200 kg cm^{-2}. The loading of each electrode was approximatly 1.2 mg. Electrochemical measurements were carried out using two-electrode coin cells (CR2032) with Na metal as reference and counter electrode and the glass microfiber (Whatman) as the separator. The CR2032 coin cells were assembled in an argon-filled glovebox (UniLab, Mbraun, Germany). The electrolyte solution was 1 M $NaClO_4$ dissolved in a mixture of ethylene carbonate and propylene carbonate with a volume ratio of 1:1. Cyclic voltammetry was carried out on a CHI 660C electrochemistry workstation with a scan rate of 0.1 mV s^{-1} from 1.0 to 4.0 V. The charge−discharge measurements were performed at ambient temperature at different current densities in the voltage range from 1.0 to 4.0 V. In order to investigate the sodium-driven structural and morphological changes of the as-prepared V_2O_5, Swagelok-type cells were assembled. The cells were discharged to the required voltages and then opened in the glovebox. The active materials were removed from the electrodes and washed with propylene carbonate before being used for *ex-situ* XRD analysis.

Conflict of Interest: The authors declare no competing financial interest.

Acknowledgment. This work was financially supported by the Australian Research Council (ARC) through the ARC FT project (FT110100800). We also acknowledge the support from the ARC Discovery project (DP1093855).

Supporting Information Available: Supplementary TEM, SEM, XRD, crystal structure, and electrochemical testing data are included. This material is available free of charge *via* the Internet at http://pubs.acs.org.

REFERENCES AND NOTES

1. Ong, S. P.; Chevrier, V. L.; Hautier, G.; Jain, A.; Moore, C.; Kim, S.; Ma, X.; Ceder, G. Voltage, Stability and Diffusion Barrier Differences between Sodium-Ion and Lithium-Ion Intercalation Materials. *Energ. Environ. Sci.* **2011**, *4*, 3680–3688.
2. Ellis, B. L.; Nazar, L. F. Sodium and Sodium-Ion Energy Storage Batteries. *Curr. Opin. Solid State Mater Sci.* **2012**, *16*, 168–177.
3. Tarascon, J. M. Key Challenges in Future Li-Battery Research. *Philos. Trans. R. Soc. A* **2010**, *368*, 3227–3241.
4. Tarascon, J. M. Is Lithium the New Gold? *Nat. Chem.* **2010**, *2*, 510–510.
5. Zaghib, K.; Trottier, J.; Hovington, P.; Brochu, F.; Guerfi, A.; Mauger, A.; Julien, C. M. Characterization of Na-Based Phosphate as Electrode Materials for Electrochemical Cells. *J. Power Sources* **2011**, *196*, 9612–9617.
6. Gocheva, I. D.; Nishijima, M.; Doi, T.; Okada, S.; Yamaki, J.; Nishida, T. Mechanochemical Synthesis of $NaMF_3$ (M = Fe, Mn, Ni) and Their Electrochemical Properties as Positive Electrode Materials for Sodium Batteries. *J. Power Sources* **2009**, *187*, 247–252.
7. Yamada, Y.; Doi, T.; Tanaka, I.; Okada, S.; Yamaki, J. Liquid-Phase Synthesis of Highly Dispersed $NaFeF_3$ Particles and Their Electrochemical Properties for Sodium-Ion Batteries. *J. Power Sources* **2011**, *196*, 4837–4841.
8. Berthelot, R.; Carlier, D.; Delmas, C. Electrochemical Investigation of The P2-Na_xCoO_2 Phase Diagram. *Nat. Mater.* **2011**, *10*, 74–U3.
9. Doeff, M. M.; Ma, Y. P.; Peng, M. Y.; Visco, S. J.; Dejonghe, L. C. Solid Sodium Solid Polymer Electrolyte Batteries. *Energy Environment Economics: 28th Intersociety Energy Conversion Engineering Conference (Iecec-93)*; **1993**; Vol. *1*, pp 1111−1116.
10. Yabuuchi, N.; Kajiyama, M.; Iwatate, J.; Nishikawa, H.; Hitomi, S.; Okuyama, R.; Usui, R.; Yamada, Y.; Komaba, S. P2-Type $Na_x[Fe_{1/2}Mn_{1/2}]O_2$ Made from Earth-Abundant Elements for Rechargeable Na Batteries. *Nat. Mater.* **2012**, *11*, 512–517.
11. Kim, D.; Lee, E.; Slater, M.; Lu, W. Q.; Rood, S.; Johnson, C. S. Layered $Na[Ni_{1/3}Fe_{1/3}Mn_{1/3}]O_2$ Cathodes for Na-Ion Battery Application. *Electrochem. Commun.* **2012**, *18*, 66–69.
12. Komaba, S.; Takei, C.; Nakayama, T.; Ogata, A.; Yabuuchi, N. Electrochemical Intercalation Activity of Layered $NaCrO_2$ *vs.* $LiCrO_2$. *Electrochem. Commun.* **2010**, *12*, 355–358.
13. Xia, X.; Dahn, J. R. $NaCrO_2$ is a Fundamentally Safe Positive Electrode Material for Sodium-Ion Batteries with Liquid Electrolytes. *Electrochem. Solid State* **2012**, *15*, A1–A4.

14. Mendiboure, A.; Delmas, C.; Hagenmuller, P. Electrochemical Intercalation and Deintercalation of Na_xMnO_2 Bronzes. *J. Solid State Chem.* **1985**, *57*, 323–331.
15. Stoyanova, R.; Carlier, D.; Sendova-Vassileva, M.; Yoncheva, M.; Zhecheva, E.; Nihtianova, D.; Delmas, C. Stabilization of Over-Stoichiometric Mn^{4+} in Layered $Na_{2/3}MnO_2$. *J. Solid State Chem.* **2010**, *183*, 1372–1379.
16. Hamani, D.; Ati, M.; Tarascon, J.-M.; Rozier, P. Na_xVO_2 as Possible Electrode for Na-Ion Batteries. *Electrochem. Commun.* **2011**, *13*, 938–941.
17. Recham, N.; Chotard, J. N.; Dupont, L.; Djellab, K.; Armand, M.; Tarascon, J. M. Ionothermal Synthesis of Sodium-Based Fluorophosphate Cathode Materials. *J. Electrochem. Soc.* **2009**, *156*, A993–A999.
18. Reynaud, M.; Barpanda, P.; Rousse, G.; Chotard, J. N.; Melot, B. C.; Recham, N.; Tarascon, J. M. Synthesis and Crystal Chemistry of the $NaMSO_4F$ Family (M = Mg, Fe, Co, Cu, Zn). *Solid State Sci.* **2012**, *14*, 15–20.
19. Barpanda, P.; Chotard, J. N.; Recham, N.; Delacourt, C.; Ati, M.; Dupont, L.; Armand, M.; Tarascon, J. M. Structural, Transport, and Electrochemical Investigation of Novel $AMSO_4F$ (A = Na, Li; M = Fe, Co, Ni, Mn) Metal Fluorosulphates Prepared Using Low Temperature Synthesis Routes. *Inorg. Chem.* **2010**, *49*, 7401–7413.
20. Ati, M.; Dupont, L.; Recham, N.; Chotard, J. N.; Walker, W. T.; Davoisne, C.; Barpanda, P.; Sarou-Kanian, V.; Armand, M.; Tarascon, J. M. Synthesis, Structural, and Transport Properties of Novel Bihydrated Fluorosulphates $NaMSO_4F$ Center Dot $2H_2O$ (M = Fe, Co, and Ni). *Chem. Mater.* **2010**, *22*, 4062–4068.
21. Su, D.; Ahn, H.-J.; Wang, G. Hydrothermal Synthesis of α-MnO_2 and β-MnO_2 Nanorods as High Capacity Cathode Materials for Sodium Ion Batteries. *J. Mater. Chem. A* **2013**, *1*, 4845–4850.
22. Su, D.; Wang, C.; Ahn, H. J.; Wang, G. Single Crystalline $Na_{0.7}MnO_2$ Nanoplates as Cathode Materials for Sodium-Ion Batteries with Enhanced Performance. *Chem.—Eur. J.* **2013**, *19*, 10884–10889.
23. Ma, X.; Chen, H.; Ceder, G. Electrochemical Properties of Monoclinic $NaMnO_2$. *J. Electrochem. Soc.* **2011**, *158*, A1307–A1312.
24. Kim, D.; Kang, S. H.; Slater, M.; Rood, S.; Vaughey, J. T.; Karan, N.; Balasubramanian, M.; Johnson, C. S. Enabling Sodium Batteries Using Lithium-Substituted Sodium Layered Transition Metal Oxide Cathodes. *Adv. Energy Mater.* **2011**, *1*, 333–336.
25. Lee, K. T.; Ramesh, T.; Nan, F.; Botton, G.; Nazar, L. F. Topochemical Synthesis of Sodium Metal Phosphate Olivines for Sodium-Ion Batteries. *Chem. Mater.* **2011**, *23*, 3593–3600.
26. Moreau, P.; Guyomard, D.; Gaubicher, J.; Boucher, F. Structure and Stability of Sodium Intercalated Phases in Olivine $FePO_4$. *Chem. Mater.* **2010**, *22*, 4126–4128.
27. Tillement, O.; Angenault, J.; Couturier, J.; Quarton, M. Electrochemical Studies of Mixed Valence NASICON. *Solid State Ionics* **1992**, *53*, 391–399.
28. Park, S. I.; Gocheva, I.; Okada, S.; Yamaki, J.-i. Electrochemical Properties of $NaTi_2(PO_4)_3$ Anode for Rechargeable Aqueous Sodium-Ion Batteries. *J. Electrochem. Soc.* **2011**, *158*, A1067–A1070.
29. Zhao, L.; Zhao, J.; Hu, Y. S.; Li, H.; Zhou, Z.; Armand, M.; Chen, L. Disodium Terephthalate ($Na_2C_8H_4O_4$) as High Performance Anode Material for Low-Cost Room-Temperature Sodium-Ion Battery. *Adv. Energy Mater.* **2012**, *2*, 962–965.
30. Cao, Y. L.; Xiao, L. F.; Sushko, M. L.; Wang, W.; Schwenzer, B.; Xiao, J.; Nie, Z. M.; Saraf, L. V.; Yang, Z. G.; Liu, J. Sodium Ion Insertion in Hollow Carbon Nanowires for Battery Applications. *Nano Lett.* **2012**, *12*, 3783–3787.
31. Goodenough, J.; Hong, H.-P.; Kafalas, J. Fast Na^+-Ion Transport in Skeleton Structures. *Mater. Res. Bull.* **1976**, *11*, 203–220.
32. Padhi, A.; Nanjundaswamy, K.; Masquelier, C.; Goodenough, J. Mapping of Transition Metal Redox Energies in Phosphates with NASICON Structure by Lithium Intercalation. *J. Electrochem. Soc.* **1997**, *144*, 2581–2586.
33. Lu, Y.; Wang, L.; Cheng, J.; Goodenough, J. B. Prussian Blue: A New Framework of Electrode Materials for Sodium Batteries. *Chem. Commun.* **2012**, *48*, 6544–6546.
34. Rui, X.; Lu, Z.; Yu, H.; Yang, D.; Hng, H. H.; Lim, T. M.; Yan, Q. Ultrathin V_2O_5 Nanosheet Cathodes: Realizing Ultrafast Reversible Lithium Storage. *Nanoscale* **2013**, *5*, 556–560.
35. Mai, L.; Dong, F.; Xu, X.; Luo, Y.; An, Q.; Zhao, Y.; Pan, J.; Yang, J. Cucumber-Like V_2O_5/poly(3,4-ethylenedioxythiophene) & MnO_2 Nanowires with Enhanced Electrochemical Cyclability. *Nano Lett.* **2013**, *13*, 740–745.
36. Tang, W.; Gao, X.; Zhu, Y.; Yue, Y.; Shi, Y.; Wu, Y.; Zhu, K. A Hybrid of V_2O_5 Nanowires and MWCNTs Coated with Polypyrrole as an Anode Material for Aqueous Rechargeable Lithium Batteries with Excellent Cycling Performance. *J. Mater. Chem.* **2012**, *22*, 20143–20145.
37. Qu, Q.; Zhu, Y.; Gao, X.; Wu, Y. Core - Shell Structure of Polypyrrole Grown on V_2O_5 Nanoribbon as High Performance Anode Material for Supercapacitors. *Adv. Energy Mater.* **2012**, *2*, 950–955.
38. Rocquefelte, X.; Boucher, F.; Gressier, P.; Ouvrard, G. First-Principle Study of the Intercalation Process in the $Li_xV_2O_5$ System. *Chem. Mater.* **2003**, *15*, 1812–1819.
39. Tepavcevic, S.; Xiong, H.; Stamenkovic, V. R.; Zuo, X.; Balasubramanian, M.; Prakapenka, V. B.; Johnson, C. S.; Rajh, T. Nanostructured Bilayered Vanadium Oxide Electrodes for Rechargeable Sodium-Ion Batteries. *ACS Nano* **2012**, *6*, 530–538.
40. Larsen, A.; Von Dreele, R. GSAS, General Structure Analysis System. *Report LAUR-86±748*; Los Alamos National Laboratory: NM, USA, 1994.
41. Rietveld, H. M. The Reitveld Method? A Historical Perspective. *Aust. J. Phys.* **1988**, *41*, 113–116.
42. Chen, W.; Xu, Q.; Hu, Y. S.; Mai, L. Q.; Zhu, Q. Y. Effect of Modification by Poly(Ethylene Oxide) on the Reversibility of Insertion/Extraction of Li^+ Ion in V_2O_5 Xerogel Films. *J. Mater. Chem.* **2002**, *12*, 1926–1929.
43. Petkov, V.; Trikalitis, P. N.; Bozin, E. S.; Billinge, S. J.; Vogt, T.; Kanatzidis, M. G. Structure of $V_2O_5 \cdot nH_2O$ Xerogel Solved by the Atomic Pair Distribution Function Technique. *J. Am. Chem. Soc.* **2002**, *124*, 10157–10162.
44. Petkov, V.; Billinge, S.; Larson, P.; Mahanti, S.; Vogt, T.; Rangan, K.; Kanatzidis, M. Structure of Nanocrystalline Materials Using Atomic Pair Distribution Function Analysis: Study of $LiMoS_2$. *Phys. Rev. B* **2002**, *65*, 092105.
45. Abello, L.; Husson, E.; Repelin, Y.; Lucazeau, G. Vibrational Spectra and Valence Force Field of Crystalline V_2O_5. *Spectrochim. Acta A* **1983**, *39*, 641–651.
46. Petrov, G. I.; Yakovlev, V. V.; Squier, J. Raman Microscopy Analysis of Phase Transformation Mechanisms in Vanadium Dioxide. *Appl. Phys. Lett.* **2002**, *81*, 1023–1025.
47. Repelin, Y.; Husson, E.; Abello, L.; Lucazeau, G. Structural Study of Gels of V_2O_5: Normal Coordinate Analysis. *Spectrochim. Acta A* **1985**, *41*, 993–1003.
48. Su, Q.; Liu, X.; Ma, H.; Guo, Y.; Wang, Y. Raman Spectroscopic Characterization of the Microstructure of V_2O_5 Films. *J. Solid State Electrochem.* **2008**, *12*, 919–923.
49. Ramana, C.; Smith, R.; Hussain, O.; Massot, M.; Julien, C. Surface Analysis of Pulsed Laser-Deposited V_2O_5 Thin Films and Their Lithium Intercalated Products Studied by Raman Spectroscopy. *Surf. Interface Anal.* **2005**, *37*, 406–411.
50. Leroux, F.; Goward, G.; Power, W.; Nazar, L. Electrochemical Li Insertion into Conductive Polymer/V_2O_5 Nanocomposites. *J. Electrochem. Soc.* **1997**, *144*, 3886–3895.
51. Harreld, J.; Wong, H. P.; Dave, B. C.; Dunn, B.; Nazar, L. F. Synthesis and Properties of Polypyrrole - Vanadium Oxide Hybrid Aerogels. *J. Non-Cryst. Solids* **1998**, *225*, 319–324.
52. Wang, G.; Liu, H.; Horvat, J.; Wang, B.; Qiao, S.; Park, J.; Ahn, H. Highly Ordered Mesoporous Cobalt Oxide Nanostructures: Synthesis, Characterisation, Magnetic Properties, and Applications for Electrochemical Energy Devices. *Chem.—Eur. J.* **2010**, *16*, 11020–11027.
53. Wu, Y.; Manthiram, A. High Capacity, Surface-Modified Layered $Li\ Li_{(1-x)/3}Mn_{(2-x)/3}Ni_{x/3}Co_{x/3}O_2$ Cathodes with

Low Irreversible Capacity Loss. *Electrochem. Solid-State Lett.* **2006**, *9*, A221–A224.
54. Chen, W.-M.; Qie, L.; Shao, Q.-G.; Yuan, L.-X.; Zhang, W.-X.; Huang, Y.-H. Controllable Synthesis of Hollow Bipyramid β-MnO_2 and Its High Electrochemical Performance for Lithium Storage. *ACS Appl. Mater. Interfaces* **2012**, *4*, 3047–3053.
55. Poizot, P.; Laruelle, S.; Grugeon, S.; Tarascon, J.-M. Rationalization of the Low-Potential Reactivity of 3d-Metal-Based Inorganic Compounds toward Li. *J. Electrochem. Soc.* **2002**, *149*, A1212–A1217.
56. Edström, K.; Gustafsson, T.; Thomas, J. O. The Cathode-Electrolyte Interface in the Li-Ion Battery. *Electrochim. Acta* **2004**, *50*, 397–403.
57. Tang, W.; Hou, Y.; Wang, F.; Liu, L.; Wu, Y.; Zhu, K. $LiMn_2O_4$ Nanotube as Cathode Material of Second-Level Charge Capability for Aqueous Rechargeable Batteries. *Nano Lett.* **2013**, *13*, 2036–2040.